scientific reports

OPEN

Optimizing encoding strategies for 4D Flow MRI of mean and turbulent flow

Pietro Dirix✉, Stefano Buoso & Sebastian Kozerke

For 4D Flow MRI of mean and turbulent flow a compromise between spatiotemporal undersampling and velocity encodings needs to be found. Assuming a fixed scan time budget, the impact of trading off spatiotemporal undersampling versus velocity encodings on quantification of velocity and turbulence for aortic 4D Flow MRI was investigated. For this purpose, patient-specific mean and turbulent aortic flow data were generated using computational fluid dynamics which were embedded into the patient-specific background image data to generate synthetic MRI data with corresponding ground truth flow. Cardiac and respiratory motion were included. Using the synthetic MRI data as input, 4D Flow MRI was subsequently simulated with undersampling along pseudo-spiral Golden angle Cartesian trajectories for various velocity encoding schemes. Data were reconstructed using a locally low rank approach to obtain mean and turbulent flow fields to be compared to ground truth. Results show that, for a 15-min scan, velocity magnitudes can be reconstructed with good accuracy relatively independent of the velocity encoding scheme ($SSIM_U = 0.938 \pm 0.003$), good accuracy ($SSIM_U \geq 0.933$) and with peak velocity errors limited to 10%. Turbulence maps on the other hand suffer from both lower reconstruction quality ($SSIM_{TKE} \geq 0.323$) and larger sensitivity to undersampling, motion and velocity encoding strengths ($SSIM_{TKE} = 0.570 \pm 0.110$) when compared to velocity maps. The best compromise to measure unwrapped velocity maps and turbulent kinetic energy given a fixed 15-min scan budget was found to be a 7-point multi-V_{enc} acquisition with a low V_{enc} tuned for best sensitivity to the range of expected intra-voxel standard deviations and a high V_{enc} larger than the expected peak velocity.

Aortic stenosis (AS), if not treated, is associated with elevated morbidity and mortality[1,2]. Timely diagnosis and treatment of AS is therefore of critical importance. However, accurately gauging the severity of the disease remains a challenge[2]. As AS is characterized by abnormal flow patterns[3–5] and irreversible pressure drops[6–9], quantifying aortic velocity and turbulence fields is considered an important readout for risk assessment and patient stratification[5,10].

Time-resolved volumetric phase-contrast magnetic resonance imaging (4D Flow MRI) has facilitated the measurement of aortic flow patterns[11,12]. Despite notable efforts in sequence design[13–15], undersampling and associated image reconstruction techniques[14,16–21], 4D Flow MRI data still suffers from limited spatiotemporal resolution and artifacts. Also, given that patients with aortic stenosis typically present with large peak velocities, single high-V_{enc} acquisitions are suboptimal due to velocity-to-noise limitations (VNR). Low-V_{enc} acquisitions allow to increase the sensitivity to velocity but require unwrapping of phase maps[22,23]. Various multi-V_{enc} approaches have been proposed to improve the precision of velocity measurements[22,24–27] and to increase the sensitivity to turbulence[13,28,29]. It is commonly accepted that increasing the number of velocity encoding points is beneficial for both turbulence and velocity quantification[28,30]. A dual-V_{enc} 7-point normal encoding proposed by Schnell et al.[22] has been shown to improve quantification of flows across a relatively large range of velocities. Additionally, Callaghan et al.[25] demonstrated that for identical scan times, multi-V_{enc} acquisitions outperform multiple averages of high single-V_{enc} scans. However, any additional velocity encoding point results in increased scan time. To counteract the scan time increase, advanced acceleration techniques have been proposed[31–33].

Although many studies exist on accelerated flow quantification using 4D Flow MRI, only few of them investigate quantification of turbulence. A single-V_{enc} 7-point ICOSA velocity encoding scheme was successfully used by Ha et al.[34] to discriminate between healthy volunteers and a stenotic patient based on turbulence indicators.

Institute for Biomedical Engineering, University and ETH Zurich, Zurich, Switzerland. ✉email: dirix@biomed.ee.ethz.ch

Walheim et al.[35] employed a highly-accelerated 19-point triple-V_{enc} encoding scheme for combined quantification of velocity and turbulence in under 10 min. The aforementioned works, however, lack access to ground-truth data and consequently, a systematic study on accuracy and precision. In particular, the interplay between encoding directions, encoding strengths, undersampling and breathing motion has not been addressed so far.

While in-vitro phantom studies have been conducted[28,36,37], the complexity of cardiac and vascular anatomy and its hemodynamics cannot be fully represented in-vitro, thereby impacting the performance of spatiotemporal undersampling and reconstruction approaches. The optimization of 4D Flow MRI therefore requires realistic biophysical simulation.

Previous works have shown both the ability to generate patient-specific simulations from MR measurements[38,39] and the feasibility of generating realistic 4D Flow MRI data associated with known ground truth which could be used in design and optimization approaches[37,40–42], especially when considering velocity and turbulence fields. Computational fluid dynamics (CFD) allows to simulate realistic blood flow in aortic shapes and, by simulating the acquisition process, corresponding MR signals can be generated, providing ground truth and 4D Flow MRI data pairs. The complex-valued magnetization can be computed by solving the Bloch equations in the Lagrangian frame of reference[43,44] which allows for the evaluation of specific MRI sequences while inherently considering flow-induced displacement and dephasing artifacts[45]. Of note, to accurately compute MRI signals for turbulent flows, tracking of a large number of material points is necessary, making these simulations computationally excessive. Alternatively, synthetic MRI images can be generated using a model equation, directly incorporating pointwise velocity and turbulence data from CFD, thereby significantly reducing the computational cost[40,46].

In the study at hand we investigate the impact of undersampling, velocity encoding strategy and breathing motion on the quantification of velocity and turbulence using a patient-specific synthetic 4D Flow MRI dataset as input.

Methods

Ground-truth velocity and turbulent flow fields were generated using CFD based on the time-resolved anatomy of a patient with aortic stenosis. Complex-valued PC-MRI data were derived using a signal model and embedded into the patient-specific background in the expiratory state. To simulate respiratory motion, the data were warped using breathing motion patterns from the patient. Subsequently, prospective sequential filling of k-space according to a pseudo-spiral Cartesian trajectory[47] was performed and data were reconstructed using a locally low-rank (LLR) approach[35,48]. The details of these steps are presented in the following paragraphs. Additional details on the method are available in the supplemental material.

Synthetic 4D Flow MRI data generation

In this work we simulated undersampled 4D Flow MRI data using the methods outlined in Fig. 1. Details on segmentation, boundary conditions and simulation of turbulent flow in the aorta can be found in our previous work[49] (Fig. 1a,b). Instantaneous CFD flow fields, including velocity and Reynolds stress tensor were downsampled to MRI resolution for each cardiac phase and cycle and a signal equation was used to synthesize 4D Flow MR data for each encoding direction n_v. Synthesized aortic data was embedded into a 4D Flow MRI background, resulting in MR images with realistic background and ground truth aortic foreground (Fig. 1c). Eight coils[29] with complex sensitivities C were simulated using the Biot-Savart law[50]. Data were converted to k-space using the Fourier transform $\mathcal{F}$. This set of fully sampled k-spaces constituted a pool of data that was prospectively undersampled and reconstructed using a locally low rank[35] approach (Fig. 1d,e). To investigate the impact of breathing motion, registration of expiratory and inspiratory states was performed on the 5D Flow MRI data and the displacement field was used on the images to impose motion (Fig. 1f).

Ground-truth data generation

A previously developed approach for personalized patient-specific CFD simulations[49] was utilized to generate data. In this study, a subject with moderate aortic stenosis[51] (echocardiographic peak velocity = 3.1 m/s) was obtained upon written informed consent and approval of the ethics committee of the Canton of Zurich, Switzerland, and according to institutional guidelines. All data were acquired on a 1.5T MR system (Philips Healthcare, Best, The Netherlands) using a cardiac receive array. The data included a 5D Flow MRI scan ($2.5 \times 2.5 \times 2.5$ mm^3, 40 ms), 9 cine balanced steady-state free precession (BSSFP) slices acquired along the ascending aorta and the arch ($1 \times 1 \times 5$ mm^3, 20 ms) and a cine 2D PC-MRI scan with three-directional velocity encoding acquired one diameter downstream of the aortic valve ($1.5 \times 1.5 \times 8$ mm^3, 20 ms). A custom-made dynamic segmentation tool was used to extract aortic lumen from cine images and generate a fully hexahedral computational mesh as well as extract inflow boundary conditions from 2D PC-MRI slices[49]. Hemodynamic simulations were performed by solving the three-dimensional, unsteady and incompressible Navier–Stokes equations in a moving domain. Blood was assumed Newtonian and incompressible with density $\rho = 1060$ kg/m^3 and kinematic viscosity $\mu = 3.5$ mPa·s. A large eddy simulation (LES) model in the arbitrary Lagrangian–Eulerian (ALE) framework as implemented in OpenFOAM® v1806 was employed. The subgrid scheme selected was the wall-adapting local-eddy viscosity (WALE) subgrid-scale (SGS) model and Spalding's wall function was used. Second-order central differences and backward Euler schemes were used for spatial and temporal discretization. Adaptive time stepping was used to reduce simulation times. A total of $N_{hb} = 30$ heart beats were simulated and $N_{cp} = 80$ cardiac phases were saved per beat. Fully-sampled 4D Flow MRI data was generated by computing magnitude and phase values as reported previously[49]. The simplified MR signal model reads:
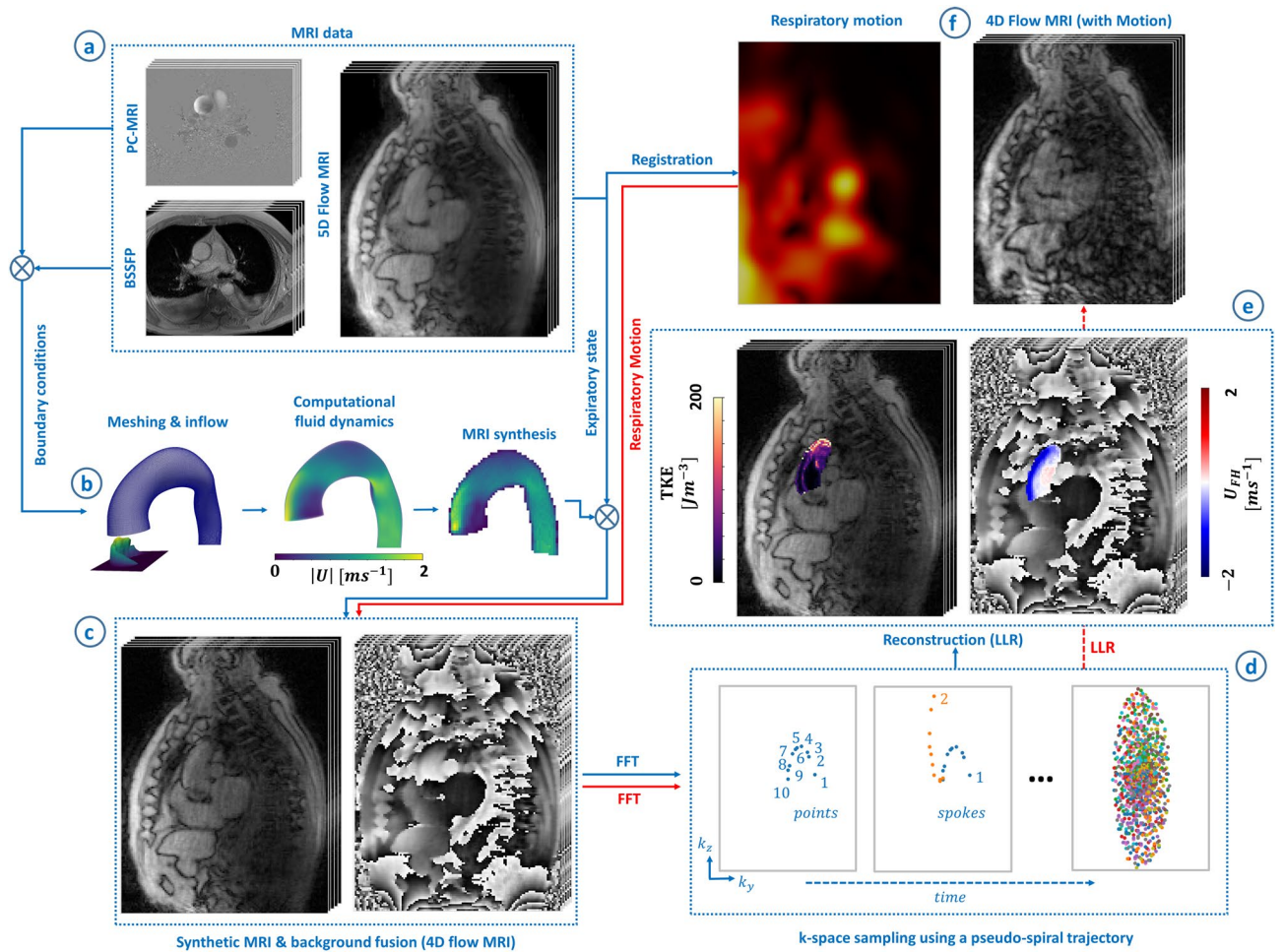
Fig. 1. Summary of the 4D Flow MRI synthesis process. (**a**) Acquisition of in-vivo MR data including cine BSSFP slices acquired along the aorta, a 2D PC-MRI slice acquired one aortic diameter downstream of the aortic valve and a 5D Flow MRI scan. (**b**) Generation of a dynamic aortic mesh based on the BSSFP slices, extraction of velocity profiles from the 2D PC-MRI slice, simulation of blood flow using CFD and synthesis of MRI signals[49]. (**c**) Embedding of simulated 4D Flow MRI of the aorta into the background extracted from the expiratory state of the respiratory-resolved 5D Flow MRI input data. (**d**) Simulated acquisition of k-space points based on a pseudo-spiral trajectory. (**e**) Reconstruction of undersampled data (LLR) and analysis of flow related fields. (**f**) Extraction of respiratory motion from registration of the expiratory and inspiratory states of the 5D Flow MRI data and subsequent application of respiratory displacement on the synthetic data to create synthetic motion corrupted 4D Flow data.

$$S\left(\boldsymbol{k}_{v,i}\right) = S_0 e^{-\frac{k_{v,i}^T R k_{v,i}}{2}} e^{-j k_{v,i} U} + \eta, \tag{1}$$

where U is the velocity vector, $\boldsymbol{R}$ is the Reynolds stress tensor, S_0 is a complex-valued reference image, $\boldsymbol{k}_{v,i} = k_{v,i} \overrightarrow{\boldsymbol{e}}_i = \left[k_{vx}, k_{vy}, k_{vz}\right]_i \in \mathbb{R}^{1 \times 3}$ represents flow sensitivity along the ith direction with encoding velocity frequency $k_{v,i} = \pi/[\mathrm{V}_{\mathrm{enc}}]_i$. η is complex Gaussian noise with zero mean and standard deviation $\sigma_\eta = \left|\bar{S}_{ROI}\right| \cdot (\mathrm{SNR})^{-1}$ with $\bar{S}_{ROI}$ being the mean noise-free signal in the region of interest, defined as the full fluid domain for all simulations. Downsampling to MR resolution was performed by projection to a fine grid ($0.65 \times 0.65 \times 0.65$ mm^3) with subsequent k-space low-pass filtering. The synthetic aortic data was then embedded back into the in-vivo 4D Flow MRI data. For all simulations, an SNR of 20 was assumed[35,52].

A reference band-limited measurement was obtained without breathing motion and without noise by downsampling cycle-to-cycle and temporally averaged CFD data[49] to MRI resolution and was used throughout the study as the target when computing error metrics.

Data undersampling and reconstruction

The fully-sampled complex-valued synthetic MRI data was undersampled as outlined in Fig. 2. For each cardiac phase n_{cp}, heart beat n_{hb} and velocity encoding point n_v, instantaneous image data $\boldsymbol{I}_t \in \mathbb{C}^{N_x \times N_y \times N_z}$ was obtained, where $N_x \times N_y \times N_z$ are the dimensions of the imaging volume. These images were then multiplied by coil sensitivity maps $\boldsymbol{C} \in \mathbb{C}^{N_x \times N_y \times N_z \times N_{coil}}$, with $N_{coil} = 8$. Upon Fourier transform, the instantaneous k-space data was obtained $\boldsymbol{S}^k \in \mathbb{C}^{N_x \times N_y \times N_z \times N_{cp} \times N_{hb} \times N_v \times N_{coil}}$, forming a pool of k-space data that was used to simulate MR
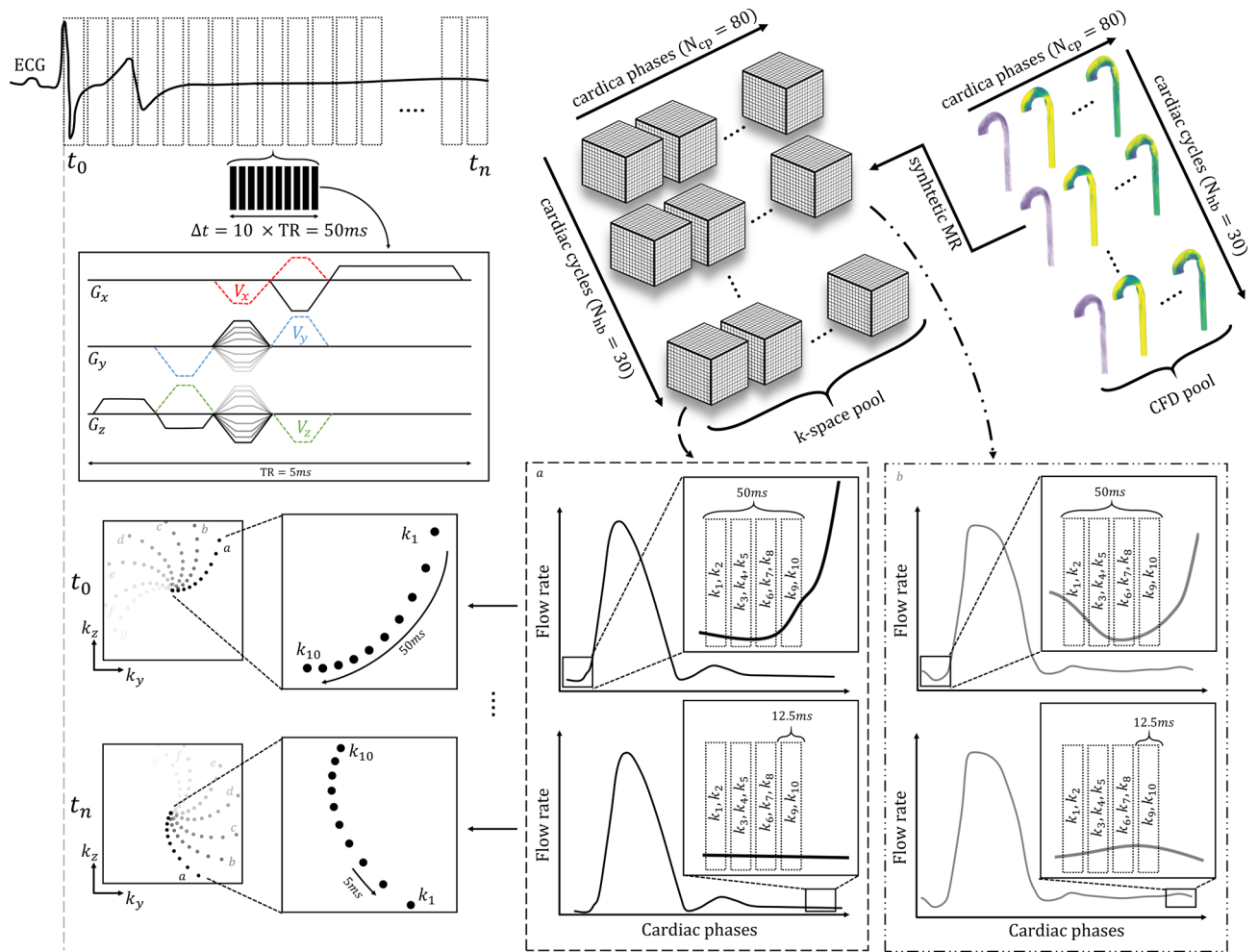
Fig. 2. Schematic of k-space sampling based on CFD based synthetic k-space data pools. A pseudo-spiral trajectory was simulated for successively acquired k-space profiles. After each cardiac cycle (**a**), a new cardiac cycle (**b**) was randomly selected to continue the acquisition. Different V_{enc} were acquired sequentially for each scan. The gradient waveform is for illustrative purposes; in this work each TR was simulated using Eq. (1).

acquisitions. A pseudo-spiral Cartesian undersampling trajectory was used to sample the k-space pool[29]. With a $T_R = 5$ ms and 10 (k_y, k_z)-samples acquired per spoke per MR cardiac phase, a temporal resolution of 50 ms was simulated. Each (k_y, k_z)-sample had an associated CFD cardiac phase and CFD cardiac cycle determined by the ordering at which each sample was acquired (for each MR cardiac phase, 4 CFD cardiac phases were used to populate 10 points in k-space, see Fig. 2). K-space was iteratively filled by sampling each k-space point in the trajectory, as shown in Fig. 2, from the target fully sampled k-space signal pool S^k. After each cardiac cycle (see Fig. 2a), a new one was randomly selected (see Fig. 2b) and the whole process was repeated until a target k-space undersampling factor was achieved. A constant RR-interval of 950 ms was assumed, resulting in a total of $N_{cp,MRI} = 19$ cardiac phases. For each acquisition, an undersampled k-space $S_u^k \in \mathbb{C}^{N_x \times N_y \times N_z \times N_{cp,MRI} \times N_v \times N_{coil}}$ was obtained. Temporal and beat-to-beat averaging was integrated into the final k-space by simulating the acquisition process which allowed to inherently include beat-to-beat variability. By repeating the acquisition of k-space 20 times using different trajectories and cardiac cycle orderings, scan-to-scan variability based on the same underlying flow can be investigated.

The undersampled k-space data was reconstructed using a locally low-rank[35] approach as implemented in the Berkeley Advanced Reconstruction Toolbox (BART)[53]:

$$\widehat{I} = argmin_I \|\mathbf{\Omega}\mathcal{F}\mathbf{C}\mathbf{I} - \mathbf{S}_u^k\|_2^2 + \lambda \sum \|R_b \mathbf{I}\|_* \tag{2}$$

where $\widehat{I}$ are the reconstructed images, $\|\blacksquare\|_*$ denotes the nuclear norm, λ is the regularization factor and the operator R_b selects the b-th out of N_b isotropic blocks of size P_b.

Multi-point six-directional velocity encoded data were processed using Bayesian multipoint unfolding[13] to obtain velocity $\mathbf{U}$, Reynolds stress tensor $\mathbf{R}$, turbulent kinetic energy $\mathbf{TKE}$ and kinetic energy $\mathbf{KE}$. In case of multi-point or single-point three-directional velocity encoding, only $\mathbf{U}$, $\mathbf{TKE}$ and $\mathbf{KE}$ could be obtained. Phase unwrapping is intrinsically included in Bayesian multipoint unfolding[13]. For standard 4-point velocity encoding, phase unwrapping using the band-limited reference was performed if required.

Undersampled synthetic data based on a 3-point feet-head dual-V_{enc} encoding ($V_{enc} = 0, 0.5, 2$ m/s, see Fig. 3) was used to test the impact of the LLR regularization parameters on global image magnitude, intra-voxel standard deviation (IVSD, σ) and velocity in the aorta. Optimal values for λ and P_b with respect to the fully sampled reference were studied using the following structural similarity indices (SSIM): $SSIM_I$, $SSIM_{u_{FH}}$ and $SSIM_{\sigma_{FH}}$; which are quality metrics based on the image magnitude ($|\hat{I}|$), feet-head velocity in the aorta (u_{FH}^A), and feet-head IVSD in the aorta (σ_{FH}^A), respectively. As shown in Table 1, optimal values of λ depend on the undersampling factor, and they range between 0.01 and 0.17, consistent with literature[16,35]. While regularization parameters are often tuned with respect to quality of the image magnitude, differences are seen depending on the target metric. When optimizing based on image magnitude ($|\hat{I}|$), $SSIM_{\sigma_{FH}}$ decreased up to 23%, when compared to optimizations for u_{FH}^A and σ_{FH}^A. Based on these results, a dual reconstruction approach was adopted in this work. The image phase
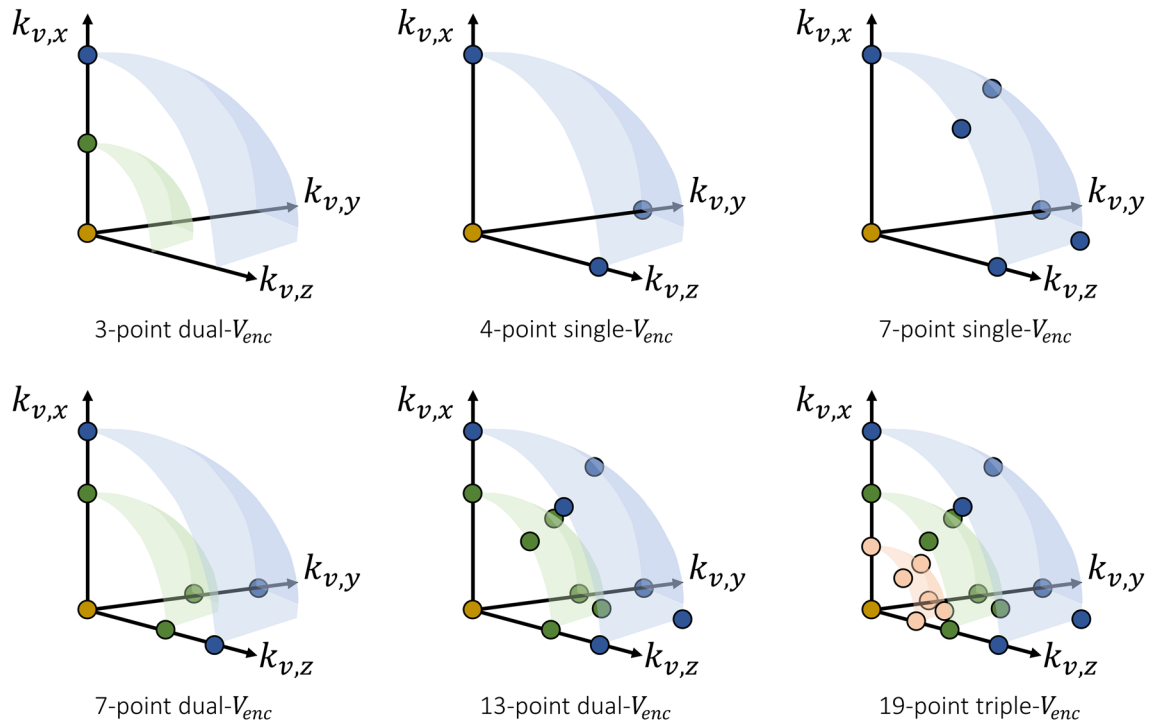

Fig. 3. Summary velocity encoding strategies including 3-point dual-V_{enc}, 4-point single-V_{enc}, 7-point single-V_{enc}, 7-point dual V_{enc}, 13-point dual-V_{enc} and 19-point triple-V_{enc}. Non diagonal terms of the Reynolds stress tensor can only be recovered if non-diagonal encoding points are included in the encoding strategy (7-point single-V_{enc}, 13-point dual-V_{enc} and 19-point triple-V_{enc}).

		$R_u = 1.93$	$R_u = 3.37$	$R_u = 6.22$	$R_u = 9.07$	$R_u = 18.14$
$|\hat{I}|$	λ	0.010	0.029	0.066	0.094	0.170
	P_b	8	32	32	32	16
	$SSIM_{u_{FH}}$	0.981	0.962	0.891	0.830	0.718
	$SSIM_{\sigma_{FH}}$	0.910	0.831	0.680	0.558	0.364
u_{FH}^A	λ	0.011	0.018	0.033	0.052	0.084
	P_b	2	2	4	8	16
	$SSIM_{u_{FH}}$	0.985	0.973	0.941	0.896	0.765
	$SSIM_{\sigma_{FH}}$	0.926	0.878	0.800	0.708	0.408
σ_{FH}^A	λ	0.013	0.023	0.037	0.052	0.110
	P_b	2	2	4	4	4
	$SSIM_{u_{FH}}$	0.985	0.972	0.940	0.888	0.729
	$SSIM_{\sigma_{FH}}$	0.926	0.880	0.803	0.718	0.471

Table 1. Summary of optimal regularization λ and block size P_b for various undersampling factors R_u and for optimal reconstructions of image magnitude ($|\mathbf{I}|$), feet-head velocity in the aorta (u_{FH}^A) and feet-head intravoxel standard deviation in the aorta (σ_{FH}^A). In this table SSIM of velocity ($SSIM_{u_{FH}}$) is the selected quality metric for u_{FH}^A and SSIM of IVSD ($SSIM_{\sigma_{FH}}$) is the quality metric for σ_{FH}^A.

was reconstructed using optimal regularization parameters for u_{FH}^A, while the magnitude was reconstructed using those for σ_{FH}^A. Exemplary optimally reconstructed images for various undersampling factors are presented in Fig. S1 of the Supplemental Material.

Respiratory motion

To obtain respiratory motion fields, the acquired 5D Flow MRI data was binned into 3 respiratory states[29,54], and the image registration toolbox pTVreg[55] was used to extract breathing-related displacement fields. A fully sampled reference scan was simulated using the approach presented in Fig. 2 and subsequently warped using the displacement fields to create 20 breathing states between end-inspiration and end-expiration. Static tissue including the spine was used to constrain deformations. The data was converted back to k-space to form a new motion informed k-space pool containing an additional dimension representing breathing motion. Motion corrupted synthetic 4D Flow MRI data was then obtained by applying the sampling approach presented in Fig. 2 on the motion informed k-space pool while additionally accounting for a simulated respiratory frequency of 0.3 Hz with a 0.04 Hz jitter. This process mimics a free-breathing acquisition. The respiratory motion amplitudes (δ_b) tested were 15, 30 and 100% of the maximum range to study the impact of respiratory binning. For 100% motion amplitude, the maximum and mean displacement of the ascending aorta were 4.6 and 3.0 mm, respectively.

Encoding strategies

Multiple encoding schemes were simulated assuming a scan time of 15 min, with V_{enc}-dependent echo times (TE) of 1.7, 1.4, and 1 ms, resulting in repetition times (TR) of 5, 4.7, and 4.3 ms for $V_{enc} = 0.5, 1$ and 2 m/s, respectively. Improved scan efficiency for $V_{enc} = 1$ and 2 m/s, within a fixed scan budget, was achieved by increasing the number of sampled k-space points by 6% and 14%, respectively, compared to an acquisition with $V_{enc} = 0.5$ m/s. For multi-V_{enc} acquisitions, a single TR must be used for all encoding points; thus, the TR and corresponding scan efficiency were set to the value corresponding to the lowest V_{enc} in the encoding scheme. Undersampling factors (R_u) assuming $V_{enc} = 0.5$ m/s were 1.93, 3.37, 6.22 and 9.07 for 4, 7, 13 and 19-point acquisitions, respectively. Single-, dual- and triple-V_{enc} encoding refer to the number of different velocity encoding strengths per encoding direction while "n-point encoding" refers to the total number of velocity encoding points. Figure 3 graphically summarizes all the encoding strategies investigated in this work.

The impact of undersampling (R_u) and breathing motion (δ_b) was studied using a dual-V_{enc} 7-point encoding ($V_{enc} = 0.5, 2m/s$) approach. Where the two V_{enc} were individually reconstructed as well as combined using Bayesian multipoint unfolding[13].

Data analysis

The assessment of image quality was based on the normalized root mean square error (nRMSE) and SSIM with a spatial Gaussian weighting[56] as implemented in Python's scikit-image library, where the target fields where obtained from the band-limited reference. Using $SSIM_U$, $SSIM_I$, $SSIM_\angle$, $SSIM_{TKE}$, $SSIM_{R_{xy}}$, $SSIM_{R_{xz}}$, and $SSIM_{R_{yz}}$ the similarity of velocity magnitude, image magnitude, image phase, TKE, and the non-diagonal terms of the Reynolds stress tensor (RST) with respect to the reference were calculated. Additionally, the vectorial normalized root-mean-square error of velocity ($\vec{U}_{rmse}$) was obtained:

$$\vec{U}_{rmse} = \sqrt{\text{mean}\left(\|U - U^I\|^2\right)/\text{mean}\left(\|U^I\|^2\right)}, \tag{3}$$

where U is the reconstructed velocity field, U^I is the reference velocity field and mean() is a spatial averaging operator in the region of interest defined by the aorta. A directional error metric ($\vec{\theta}_{err}$) was also defined[21]:

$$\vec{\theta}_{err} = \text{mean}\left(1 - \frac{|U \cdot U^I|}{\|U\|\|U^I\|}\right) \tag{4}$$

Velocity related metrics included peak velocity (U_{max}), divergence ($\nabla \cdot U$), kinetic energy integrated across the aorta (iKE) and velocity-to-noise ratio (VNR)[28] defined as:

$$VNR = \overline{\|U\|} \cdot \|U\|_\sigma^{-1}, \tag{5}$$

where $\overline{\|U\|}$ is the velocity magnitude averaged across multiple scanning repetitions and $|U|_\sigma$ is the corresponding standard deviation. VNR measures scan-to-scan variability of velocity. Turbulent kinetic energy in [J/m³] was defined as:

$$\text{TKE} = \frac{1}{2}\text{Tr}(R). \tag{6}$$

Note that computation of TKE does not require the knowledge of the whole RST, as only the diagonal terms are needed. Hence, for a normal encoding scheme with 3 directions TKE was obtained as:

$$\text{TKE} = \frac{1}{2}\left(\sigma_{k_{v,x}}^2 + \sigma_{k_{v,y}}^2 + \sigma_{k_{v,z}}^2\right), \tag{7}$$

where σ_{k_v} represents the intra-voxel standard deviation (IVSD) along the main directions. We also analyzed integrated TKE (iTKE) in [mJ] obtained by integrating TKE across the aorta. In order to measure scan-to-scan variability of TKE, we define the turbulence-to-noise ratio (TNR)[28]:

$$TNR = \overline{TKE} \cdot TKE_\sigma^{-1}, \tag{8}$$

where $\overline{TKE}$ is TKE averaged across multiple scanning repetitions and TKE_σ is the corresponding standard deviation of TKE such that a large TNR corresponds to low scan-to-scan variability. All velocity and turbulence related metrics are reported for a single cardiac phase corresponding to the largest iKE and iTKE, respectively.

Results

Impact of encoding strategy

Flow metrics are summarized in Fig. 4. With respect to CFD ground-truth, the band-limited reference yields an underestimation of U_{max} and iKE by 5 and 14%, respectively, while iTKE is overestimated by 96% due to partial volume effects and intravoxel phase dispersion caused by velocity gradients[49]. For the undersampled MRI, U_{max} varied between 1.965 and 2.070 ms^{-1} and mean $SSIM_U$, $\vec{U}_{rmse}$ and $\vec{\theta}_{err}$ were in the range [0.933, 0.943], [14.966, 17.284], and [3.398, 4.278], respectively. With respect to the band-limited reference, errors in iKE varied between 2.6 and 20.8% while errors in iTKE varied between −22.1 and 62.9%.

Mean $SSIM_{TKE}$ varied between 0.323 and 0.680. Arrow (c) in Fig. 4 highlights the significant influence of a poorly chosen V_{enc} on turbulence quantification. Values of $SSIM_{R_{xy}}$, $SSIM_{R_{xz}}$ and $SSIM_{R_{yz}}$ varied between 0.085 and 0.322. VNR and TNR were directly proportional to the chosen V_{enc}, as indicated by arrows (a) and (b) in Fig. 4. Maximum VNR and TNR were obtained for a 7-point encoding scheme with $V_{enc} = 0.5$ m/s and a 4-point encoding scheme with $V_{enc} = 0.5$ m/s, respectively. Minimum values were obtained using a 4-point encoding scheme with $V_{enc} = 2$ m/s for VNR and a 7-point encoding scheme with $V_{enc} = 2$ m/s for TNR. Examples of reconstructed flow fields can be found in Figs. S2, S3 and S4 in the Supplemental Material.

Impact of undersampling

A dual-V_{enc} 7-point encoding scheme with $V_{enc} = 0.5$ and 2 m/s was simulated (including rescans) to study the impact of various undersampling factors. The results are summarized in Fig. 5, including individual reconstructions for each V_{enc} and Bayesian combination of both encodings. For the case with $V_{enc} = 0.5$ m/s, mean $SSIM_{TKE}$ decreased from 0.680 to 0.448 when considering undersampling factors from 1.93 to 18.14, while mean $SSIM_U$ decreased from 0.933 to 0.886. Mean $\vec{U}_{rmse}$, $\vec{\theta}_{err}$ and $\nabla \cdot \boldsymbol{U}$ increased from 17.260 to 22.795, 3.844 to 5.077 and 8.937 to 14.113, respectively. Similarly, a decrease of 65.5 and 41.2% in VNR and TNR was observed. Undersampling factor also directly correlated to iTKE increase, with an overestimation up to a 40.6% when moving from $R_u = 1.93$ to $R_u = 18.14$. Mean peak velocities between 2.065 and 1.981 ms^{-1} were obtained for all reconstructions with $V_{enc} = 0.5$ m/s. On the other hand, reconstructions with $V_{enc} = 2 m/s$ resulted in mean peak velocities between 2.0 and 1.697 ms^{-1}, as pointed by arrow (a) in Fig. 5, equivalent to an underestimation of U_{max} of up to 17.8%. In general, high-V_{enc} acquisitions were of lower quality than their low-V_{enc} counterparts. The addition of regularization in undersampled images ($R_u \leq 9.07$) contributes to smoother fields, as can be seen with arrow (b) in Fig. 5, for the case of $\nabla \cdot \boldsymbol{U}$.

Impact of breathing motion

In order to estimate the influence of motion of flow quantification, a dual-V_{enc} 7-point encoding scheme with $V_{enc} = 0.5$ and 2 m/s was simulated (without rescans) including respiratory motion for various undersampling factors; the results are summarized in Figs. 6 and 7. Individual V_{enc} reconstructions as well as Bayesian combination were included. VNR and TNR measurements are not presented as only single scans were simulated. For the case with $V_{enc} = 0.5$ m/s, mean $SSIM_{TKE}$ decreased from 0.636 to 0.498 when considering respiratory motion ranges from 0 to 100%, mean $SSIM_U$ decreased from 0.926 to 0.898, and mean $\vec{U}_{rmse}$, $\vec{\theta}_{err}$ and $\nabla \cdot \boldsymbol{U}$ increased from 17.775 to 19.871, 4.050 to 4.255, and 9.301 to 10.902, respectively. Peak velocities between 2.048 and 1.994 ms^{-1} were obtained for all respiratory motion ranges. On the other hand, reconstructions with $V_{enc} = 2$ m/s resulted in peak velocities between 1.958 and 1.856 ms^{-1}, equivalent to an underestimation of U_{max} up to 10.1%. In the case of $V_{enc} = 0.5$ m/s, a motion range of 30% resulted in differences for $SSIM_U$, $SSIM_{TKE}$ and U_{max} of + 1.2, + 0.3 and − 1.3%, respectively, when compared to a motionless acquisition. On the other hand, a motion range of 100% resulted in differences of − 1.9, − 20.4 and − 2.6%. For $V_{enc} = 2$ m/s, differences with $\delta_b = 30\%$ amounted to − 0.8, + 2.8 and − 2.8%, while with $\delta_b = 100\%$ they were − 8.6, − 37.7 and − 5.2%. For all undersampling factors, flow quality metrics were lower when comparing simulations with $\delta_b = 100\%$ (Fig. 7) and simulations without respiratory motion[57,58] (Fig. 5). Only U_{max} correlated linearly with increase of breathing motion (see Fig. 6: arrow (a)), other metrics were only mildly affected when δ_b was assumed between 0 and 30% (see Fig. 6: arrow (b)). Exemplary reconstructed velocity and TKE maps for various degrees of undersampling and $\delta_b = 100\%$ are presented in Fig. S5 in the Supplemental Material. Figure 7 presents the impact of undersampling on simulated data with $\delta_b = 100\%$. Arrows (a) and (b) demonstrate the negative impact of undersampling on the resulting reconstructed data.

Discussion

In this work we investigated the impact of encoding strategies on quantification of flow and turbulence. We combined ground truth simulated patient-specific aortic foreground data with patient-specific backgrounds to simulate realistic 4D Flow MRI without and with respiratory motion.

Our results confirmed that regularization parameters depend on the target reconstruction metric and the undersampling factor (Table 1). In particular, optimizing regularization on the image magnitude alone can lead to significant errors in reconstructed flow fields. For undersampling factors of up to 9, variations in $SSIM_{u_{FH}}$ and $SSIM_{\sigma_{FH}}$ were less than 2% between the two optimal parameter sets used, suggesting that simultaneous reconstruction of phase and magnitude with a fixed setting of regularization parameters can be adequate.
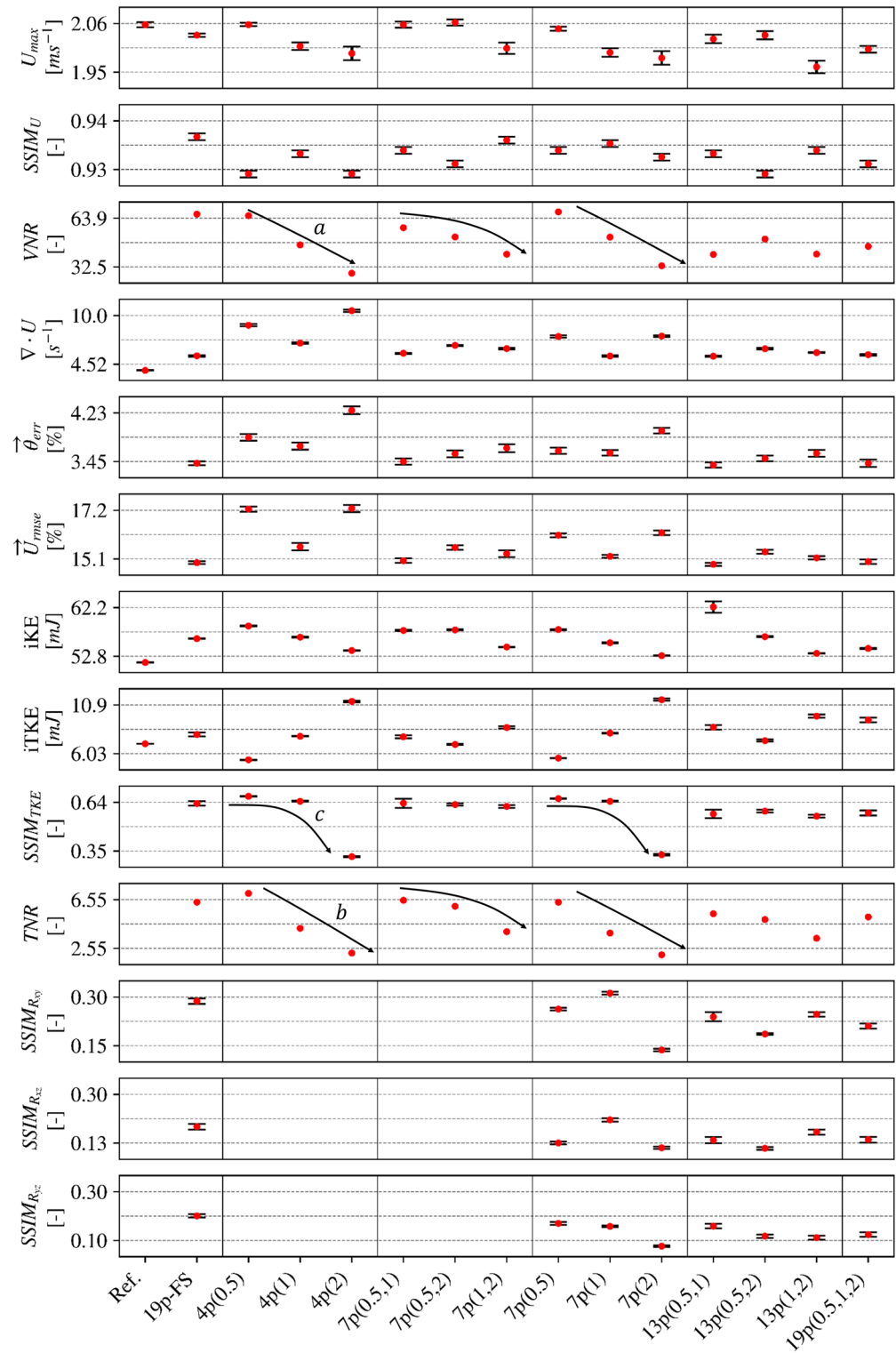
Fig. 4. Flow metrics depending on the encoding strategy. The horizontal axis lists the encoding strategies; e.g. "4p(1)" refers to a 4-point encoding scheme with a single V_{enc} of 1 m/s. In particular, Ref. and 19p-FS correspond to the band-limited reference and the 19-point fully sampled scans, respectively. Peak velocity (U_{max}), integrated kinetic energy (iKE), velocity-to-noise ratio (VNR), SSIM of velocity ($SSIM_U$), integrated turbulent kinetic energy (iTKE), turbulence-to-noise ratio (TNR) and SSIM values of TKE and non-diagonal RST terms ($SSIM_{TKE}$, $SSIM_{R_{xy}}$, $SSIM_{R_{xz}}$, $SSIM_{R_{yz}}$) are shown. In the CFD ground-truth, values for U_{max}, iTKE and iKE were 2.17 ms^{-1}, 3.548 mJ and 60.297 mJ, respectively. Additional data can be found in Tables S1 and S2 in the Supplemental Material. A video representing reconstructed flow fields and error metrics for some of the encoding strategies is available in the online Supplemental Material.
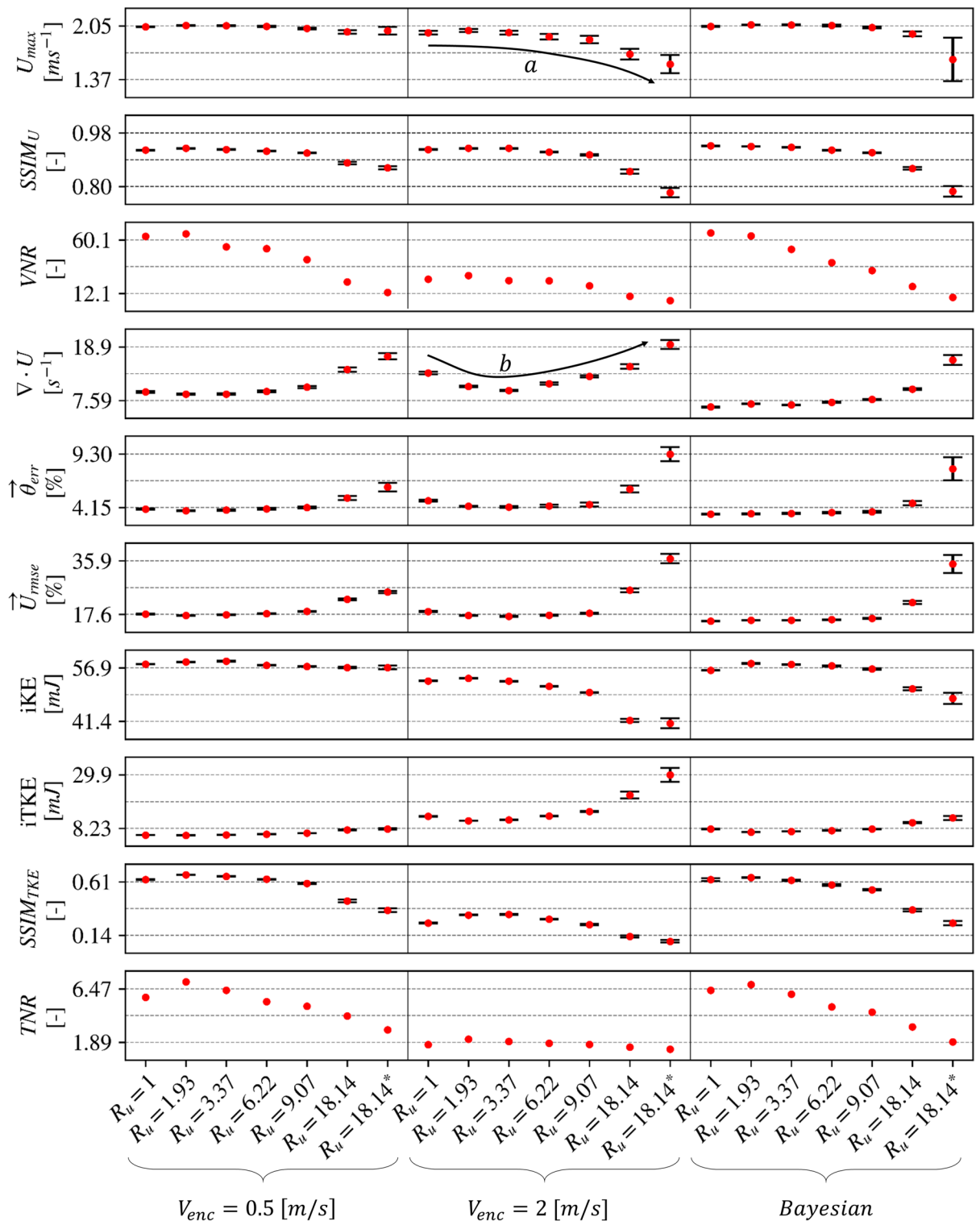
Fig. 5. Flow and turbulence metrics depending on the undersampling factor for two 4-point acquisitions with V_{enc} = 0.5 and 2 m/s, respectively. The Bayesian combination of these measurements is also presented. The * indicates reconstructions performed using a single coil. Additional data can be found in Table S3 in the Supplemental Material. In the CFD ground-truth, values for U_{max}, iTKE and iKE were 2.17 ms^{-1}, 3.548 mJ and 60.297 mJ, respectively.

Figure 4 shows that, for a fixed scan time of 15 min, high quality reconstructed velocity maps ($SSIM_U \geq 0.933$, $\vec{U}_{rmse} \leq 17.284$, $\vec{\theta}_{err} \leq 4.278$) can be obtained for all tested encoding schemes, independently of the number
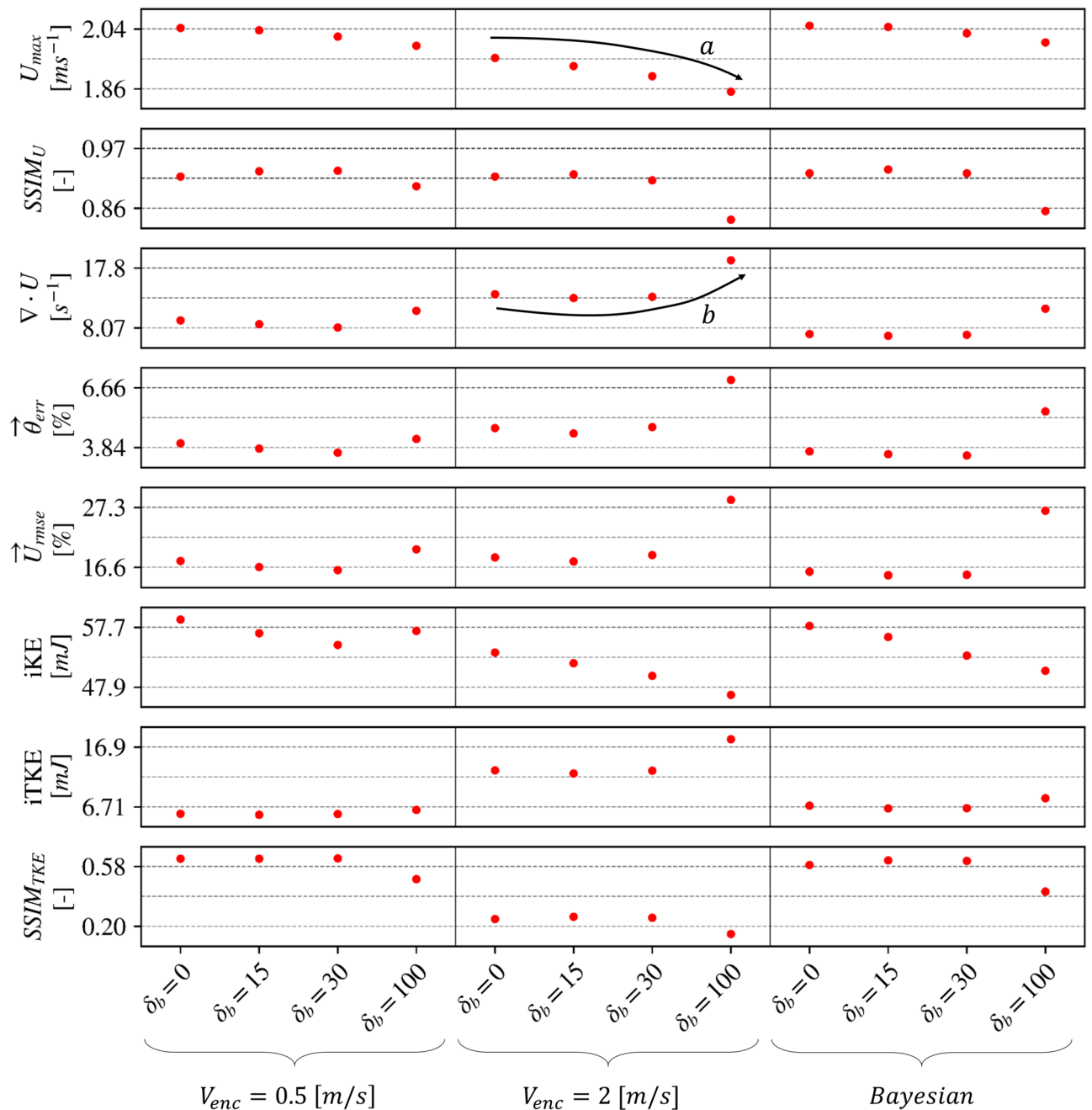
Fig. 6. Flow and turbulence metrics for a fully-sampled scan depending on respiratory motion range (δ_b) for two 4-point acquisitions with $V_{enc} = 0.5$ and 2 m/s, respectively. The Bayesian combination of these measurements is also presented. A single acquisition was simulated. Additional data can be found in Table S4 in the supplemental material. In the CFD ground-truth, values for U_{max}, iTKE and iKE were 2.17 ms^{-1}, 3.548 mJ and 60.297 mJ, respectively.

of encoding points and strengths. These results, however, assumed perfect unwrapping for the low-V_{enc} acquisitions. Contrarily to velocity fields, $SSIM_{TKE}$ values were highly sensitive to the chosen encoding strategy with overestimation of $iTKE$ as high as 223% with respect to CFD. Ha et al.[28] argued that undersampled measurements inevitably yield statistically non-converged turbulence fields, causing discrepancies with respect to ground truth. The lower intensity of fluctuations in high-velocity regions might explain why this effect was less observable for velocity maps. This aspect also affected VNR and TNR; the larger the undersampling and V_{enc}, the lower the values of these metrics[28].

The velocity encoding strength had a large impact on IVSD estimation, and based on our results, V_{enc} values between 0.3 and 0.8 m/s allowed to capture the dynamic range of voxel-wise IVSD (where optimal sensitivity to IVSD was obtained assuming $V_{enc}^{ij} = \sigma_{ij}\pi$)[35]. The range of IVSD in the aorta is case-specific and depends on the pathology. Therefore, methods to better estimate this range would facilitate the choice of V_{enc}. In our case, IVSD
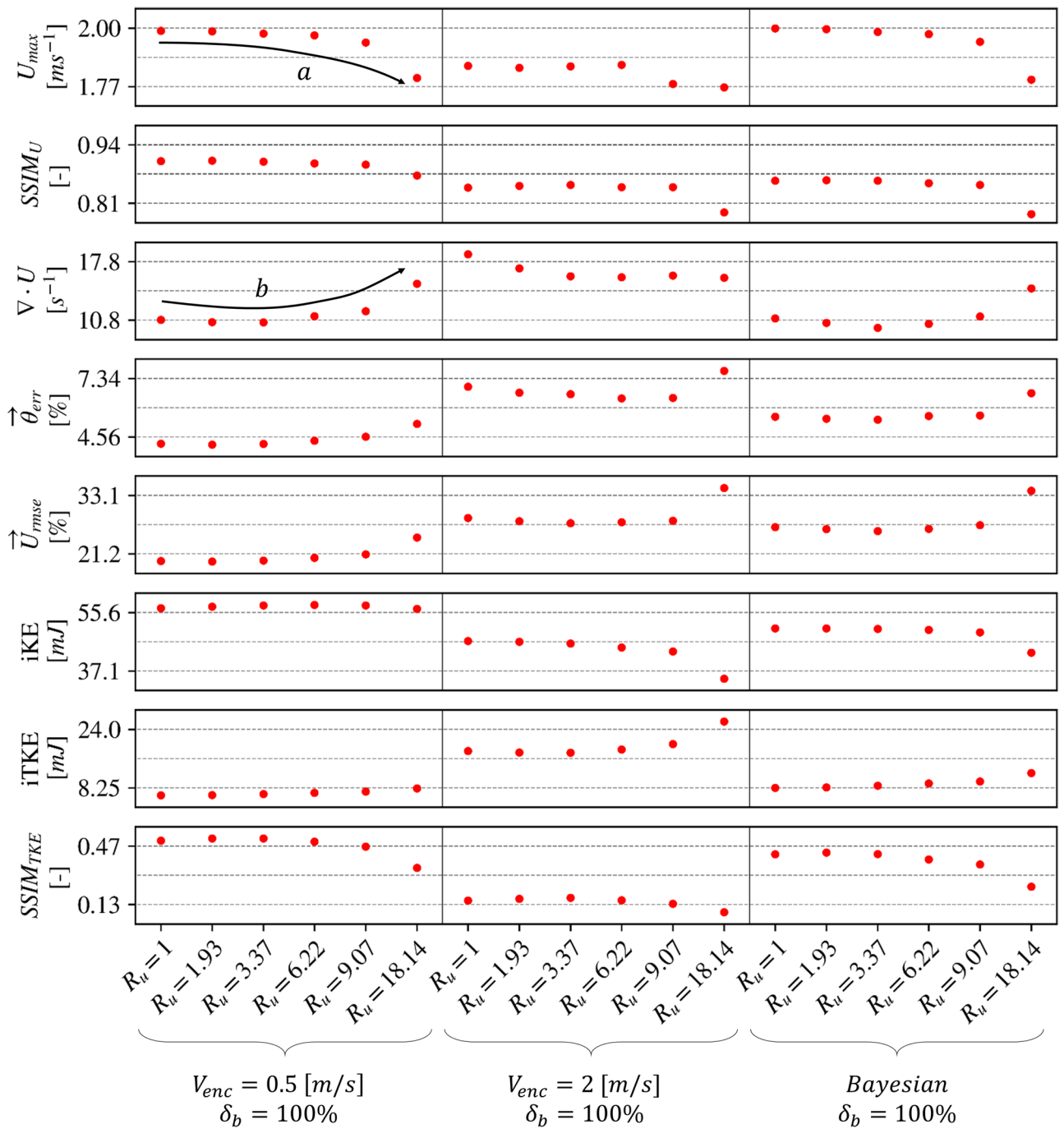
Fig. 7. Flow and turbulence metrics depending on the undersampling factor considering complete breathing motion ($\delta_b = 100\%$) for two 4-point acquisitions with $V_{enc} = 0.5$ and 2 m/s, respectively. The Bayesian combination of these measurements is also presented. A single acquisition was simulated. Additional data can be found in Table S4 in the supplemental material. In the CFD ground-truth, values for U_{max}, iTKE and iKE were 2.17 ms^{-1}, 3.548 mJ and 60.297 mJ, respectively. A video representing reconstructed flow fields and error metrics for some of the data presented here and in Figs. 5 and 6 is available in the online supplemental material.

was underestimated for $V_{enc} = 0.5$ m/s and overestimated for $V_{enc} = 1$ m/s while the map was dominated by noise for $V_{enc} = 2$ m/s. Bayesian unfolding allowed to combine measurements acquired with different encoding strengths. However, the presence of high V_{enc} values can be detrimental to the data combination process, particularly for turbulence metrics. In the case of a multi-V_{enc} 7-point acquisition ($V_{enc} = 0.5, 2$ m/s) with undersampling factor $R_u = 3.37$, the corresponding $SSIM_{TKE}$ and iTKE were 0.631 and 6.965 mJ ($+96\%$ vs CFD), respectively. The same acquisition using a single-V_{enc} 7-point acquisition ($V_{enc} = 0.5$ m/s) resulted in $SSIM_{TKE}$ and iTKE values of 0.666 and 5.594 mJ ($+58\%$ vs CFD). The penalization comes from the inclusion of acquisitions with noise-dominated IVSD maps. We also point out that choosing a V_{enc} that underestimates peak IVSD does not

necessarily mean that that iTKE will be underestimated, as limited temporal and spatial MR resolutions tend to cause overestimation of IVSD.

Reconstructed R_{xy}, R_{xz} and R_{yz} maps in this work presented SSIM values between 0.085 and 0.322, significantly lower than $SSIM_{TKE}$ and $SSIM_U$. The low quality of these maps casts doubt on the ability to use them to accurately compute flow metrics[28,40,44,59,60].

By comparing metrics from a fixed scan budget 7-point ($V_{enc} = 0.5$ m/s) to a 4-point ($V_{enc} = 0.5$ m/s) acquisition, VNR and $SSIM_U$ improved by 3.7 and 0.8%, respectively, while $\vec{U}_{rmse}$ and $\vec{\theta}_{err}$ decreased by 6.3 and 5.7%, respectively. Similarly, TNR and $SSIM_{TKE}$ decreased by 10.2 and 2.1%, respectively. Therefore, the benefit of additional encoding directions improved velocity quantification for some metrics but did not compensate for the drawback of increased undersampling in the case of turbulence.

For all the scenarios tested in this work, low-V_{enc} acquisitions demonstrated superior values of $SSIM_U$, $SSIM_{TKE}$, VNR, TNR and estimation of U_{max}. However, this superiority can only be exploited if accurate unwrapping of the phase is achievable (Supplementary Fig. S6). Bayesian combination was able to unwrap phases for all undersampling factors with 6% of residual wrapped voxels and U_{max} underestimation of up to 6.5% when compared to ground truth.

We also observed VNR values that were generally an order of magnitude greater than TNR values, suggesting that voxel-wise scan-to-scan repeatability was significantly higher for velocity measurements compared to turbulence measurements. It is important to mention that TNR values presented in this work were averaged across the aorta; in practice, TNR is spatially dependent and typically higher in regions of high turbulence. However, the use of spatially averaged TNR values allowed us to nonetheless compare sequences. These observations were also valid for VNR.

Simulated respiratory motion for single-V_{enc} 4-point acquisitions allowed us to investigate the impact of binning on 5D Flow MRI. For a low-V_{enc} and high-V_{enc} acquisitions, turbulence and velocity metrics remained within a 8.9% error when assuming $\delta_b = 30\%$, compared to a motionless reference. Similarly, the difference increases to up to 55.8% when δ_b was assumed to be 100%. This might suggest that binning respiratory motion into 3 states provides sufficient respiratory resolution to contain errors to acceptable levels. By binning respiratory motion into equal bins in terms of displacement, the range of mean ascending aortic motion reduced to 1.0mm, a sub-voxel (2.5 mm) displacement.

A limitation of this study is the use of a single patient-specific case, due to the large computational cost for simulating ground truth ($20e^3$ CPU-hours and 0.62TB), storing the k-space pool (1.98TB) and storing individual k-space realizations (4.38GB). Although the errors computed in this work are case specific and would change when considering different flow conditions, the performance of each encoding scheme should not be affected drastically if the ratios between flow velocity and V_{enc} are kept approximately the same. Also, the implementation of more complex approaches such as Eulerian–Lagrangian Bloch simulations would allow to include artifacts and sequence-specific features, but will further increase the computational cost of MRI synthesis[43,44,61–64]. Additionally, only pseudo-spiral Cartesian trajectories with LLR reconstructions were tested. Alternative reconstruction approaches for highly undersampled 4D Flow MRI data such as TV[29], k-t SPARSE SENSE[19] and FlowVN[16] can be used. Since LLR has been shown to be a good reference in some of the works, the results presented in this work are considered to be a good benchmark for a given undersampling factor. On the other hand, in the case of non-Cartesian radial[65] or spiral[66] trajectories, the inherent differences in k-space sampling with respect to Cartesian approaches might result in different spatiotemporal averaging that could affect, in particular, turbulence quantification. Further work is needed to quantify these differences. Finally, only a single SNR value was tested. For the 4-point acquisition with $V_{enc} = 2$ m/s, VNR values in this work are in agreement with in-vivo[67] and in-vitro[28] measurements. Similarly, TNR values are in agreement with in-vitro[28], suggesting that the noise level present in the dataset is adequate to represent realistic acquisitions. Since previous work has demonstrated the correlation between velocity and turbulence quantification and SNR[35,49], we can reasonably expect that for the case of equal scan budgets, variations in SNR would lead to scaling of errors in hemodynamic parameters without impacting the general conclusions of this work. The effect of SNR on a fully sampled scan is presented in Supplementary Fig. S7.

To conclude, low-V_{enc} acquisitions generally showed improvements in all quality metrics both for velocity and turbulence. However, unwrapping becomes increasingly difficult when noise, undersampling and high velocity gradients are present, compromising the potential usability of these acquisitions. Additional encoding directions improved velocity quantification but penalized turbulence measurement. In particular, the ability to measure non-diagonal terms of the RST by exploiting the additional encoding directions was negated by the low data quality obtained ($SSIM_{R_{xy}} < 0.248$, $SSIM_{R_{xz}} < 0.214$ and $SSIM_{R_{yz}} < 0.176$). Considering these results, we recommend to use dual-V_{enc} 7-point normal encoding with a low-V_{enc} ideally tuned to the expected IVSD with highest likelihood and a high V_{enc} larger than the expected U_{max}. Adopting a dual-V_{enc} 7-point normal encoding scheme allows to limit undersampling to acceptable levels when considering respiratory motion. If 3 respiratory bins are reconstructed, as suggested by our results, the effective undersampling increases by a factor of 3, resulting in $R_u \sim 10.1$ for a 15 min scan. Bayesian combination ($R_u = 9.07$) allowed to extract unwrapped velocity fields and obtain an $SSIM_U$ of 0.919 (VNR = 32.868), a $\vec{U}_{rmse}$ of 16.278%, a $\vec{\theta}_{err}$ of 3.731%, an $SSIM_{TKE}$ of 0.547 (TNR = 4.473) and a U_{max} underestimation of 1.3%. Additionally, the low-V_{enc} acquisition provided an improved $SSIM_{TKE}$ of 0.604 (TNR = 5.0). Compared to a similar fully sampled acquisition (~ 136 min), $SSIM_U$, VNR, $SSIM_{TKE}$ and TNR were inferior by 2.648, 50.569, 14.129, and 29.537%, respectively. A comparison between the proposed encoding and CFD is presented in Supplemental Fig. S8 and a video is available in the online Supplemental Material.

Data availability

The dataset generated during and/or analyzed during the current study is available from the corresponding author on reasonable request.

References

1. Dweck, M. R., Boon, N. A. & Newby, D. E. Calcific aortic stenosis. *J. Am. Coll. Cardiol.* **60**, 1854–1863 (2012).
2. Thoenes, M. *et al.* Patient screening for early detection of aortic stenosis (AS)—Review of current practice and future perspectives. *J. Thorac. Dis.* **10**, 5584–5594 (2018).
3. Saitta, S. *et al.* Evaluation of 4D Flow MRI-based non-invasive pressure assessment in aortic coarctations. *J. Biomech.* **94**, 13–21 (2019).
4. Feneis, J. F. *et al.* 4D Flow MRI quantification of mitral and tricuspid regurgitation: Reproducibility and consistency relative to conventional MRI. *J. Magn. Reson. Imaging* **48**, 1147–1158 (2018).
5. Garcia, J., Barker, A. J. & Markl, M. The role of imaging of flow patterns by 4D Flow MRI in aortic stenosis. *JACC Cardiovasc. Imaging* **12**, 252–266 (2019).
6. Dyverfeldt, P., Hope, M. D., Tseng, E. E. & Saloner, D. Magnetic resonance measurement of turbulent kinetic energy for the estimation of irreversible pressure loss in aortic stenosis. *JACC Cardiovasc. Imaging* **6**, 64–71 (2013).
7. Ha, H. *et al.* Estimating the irreversible pressure drop across a stenosis by quantifying turbulence production using 4D Flow MRI. *Sci. Rep.* **7**, 1–14 (2017).
8. Marlevi, D. *et al.* Non-invasive estimation of relative pressure in turbulent flow using virtual work-energy. *Med. Image Anal.* **60**, 101627 (2020).
9. Zhuang, B., Sirajuddin, A., Zhao, S. & Lu, M. The role of 4D Flow MRI for clinical applications in cardiovascular disease: Current status and future perspectives. *Quant. Imaging Med. Surg.* **11**, 4193–4210 (2021).
10. Binter, C. *et al.* Turbulent kinetic energy assessed by multipoint 4-dimensional flow magnetic resonance imaging provides additional information relative to echocardiography for the determination of aortic stenosis severity. *Circ. Cardiovasc. Imaging* **10**, e005486 (2017).
11. Markl, M., Frydrychowicz, A., Kozerke, S., Hope, M. & Wieben, O. 4D Flow MRI. *J. Magn. Reson. Imaging* **36**, 1015–1036 (2012).
12. Bissell, M. M. *et al.* 4D Flow cardiovascular magnetic resonance consensus statement: 2023 update. *J. Cardiovasc. Magn. Reson.* **25**, 40 (2023).
13. Binter, C., Knobloch, V., Manka, R., Sigfridsson, A. & Kozerke, S. Bayesian multipoint velocity encoding for concurrent flow and turbulence mapping. *Magn. Reson. Med.* **69**, 1337–1345 (2013).
14. Ma, L. E. *et al.* Aortic 4D Flow MRI in 2 minutes using compressed sensing, respiratory controlled adaptive k-space reordering, and inline reconstruction. *Magn. Reson. Med.* **81**, 3675–3690 (2019).
15. Wiesemann, S. *et al.* Impact of sequence type and field strength (1.5, 3, and 7T) on 4D Flow MRI hemodynamic aortic parameters in healthy volunteers. *Magn. Reson. Med.* **85**, 721–733 (2021).
16. Vishnevskiy, V., Walheim, J. & Kozerke, S. Deep variational network for rapid 4D Flow MRI reconstruction. *Nat. Mach. Intell.* **2**, 228–235 (2020).
17. Minderhoud, S. C. S. *et al.* The clinical impact of phase offset errors and different correction methods in cardiovascular magnetic resonance phase contrast imaging: A multi-scanner study. *J. Cardiovasc. Magn. Reson.* **22**, 68 (2020).
18. Partin, L., Schiavazzi, D. E. & Sing Long, C. A. An analysis of reconstruction noise from undersampled 4D Flow MRI. *Biomed. Signal Process. Control* **84**, 104800 (2023).
19. Valvano, G. *et al.* Accelerating 4D Flow MRI by exploiting low-rank matrix structure and hadamard sparsity. *Magn. Reson. Med.* **78**, 1330–1341 (2017).
20. Nath, R., Callahan, S., Stoddard, M. & Amini, A. A. FlowRAU-Net: Accelerated 4D Flow MRI of aortic valvular flows with a deep 2D residual attention network. *IEEE Trans. Biomed. Eng.* **69**, 3812–3824 (2022).
21. Santelli, C. *et al.* Accelerating 4D Flow MRI by exploiting vector field divergence regularization. *Magn. Reson. Med.* **75**, 115–125 (2016).
22. Schnell, S. *et al.* Accelerated dual-venc 4D Flow MRI for neurovascular applications. *J. Magn. Reson. Imaging* **46**, 102–114 (2017).
23. Loecher, M., Schrauben, E., Johnson, K. M. & Wieben, O. Phase unwrapping in 4D MR flow with a 4D single-step Laplacian algorithm. *J. Magn. Reson. Imaging* **43**, 833–842 (2016).
24. Ha, H. *et al.* Multi-VENC acquisition of four-dimensional phase-contrast MRI to improve precision of velocity field measurement. *Magn. Reson. Med.* **75**, 1909–1919 (2016).
25. Callaghan, F. M. *et al.* Use of multi-velocity encoding 4D Flow MRI to improve quantification of flow patterns in the aorta. *J. Magn. Reson. Imaging* **43**, 352–363 (2016).
26. Kroeger, J. R. *et al.* Velocity quantification in 44 healthy volunteers using accelerated multi-VENC 4D Flow CMR. *Eur. J. Radiol.* **137**, 109570 (2021).
27. Knobloch, V., Binter, C., Kurtcuoglu, V. & Kozerke, S. Arterial, venous, and cerebrospinal fluid flow: Simultaneous assessment with bayesian multipoint velocity-encoded MR imaging. *Radiology* **270**, 566–573 (2014).
28. Ha, H., Park, K. J., Dyverfeldt, P., Ebbers, T. & Yang, D. H. In vitro experiments on ICOSA6 4D Flow MRI measurement for the quantification of velocity and turbulence parameters. *Magn. Reson. Imaging* **72**, 49–60 (2020).
29. Walheim, J., Dillinger, H. & Kozerke, S. Multipoint 5D flow cardiovascular magnetic resonance—Accelerated cardiac- and respiratory-motion resolved mapping of mean and turbulent velocities. *J. Cardiovasc. Magn. Reson.* **21**, 42 (2019).
30. Ha, H. & Park, H. Comparison of turbulent flow measurement schemes for 4D Flow MRI. *J. Vis.* **22**, 541–553 (2019).
31. Peper, E. S. *et al.* Highly accelerated 4D Flow cardiovascular magnetic resonance using a pseudo-spiral Cartesian acquisition and compressed sensing reconstruction for carotid flow and wall shear stress. *J. Cardiovasc. Magn. Reson.* **22**, 7 (2020).
32. Liu, J., Dyverfeldt, P., Acevedo-Bolton, G., Hope, M. & Saloner, D. Highly accelerated aortic 4D Flow MR imaging with variable-density random undersampling. *Magn. Reson. Imaging* **32**, 1012–1020 (2014).
33. Pathrose, A. *et al.* Highly accelerated aortic 4D Flow MRI using compressed sensing: Performance at different acceleration factors in patients with aortic disease. *Magn. Reson. Med.* **85**, 2174–2187 (2021).
34. Ha, H. *et al.* In-vitro and in-vivo assessment of 4D Flow MRI Reynolds stress mapping for pulsatile blood flow. *Front. Bioeng. Biotechnol.* **9**, 774954 (2021).
35. Walheim, J., Dillinger, H., Gotschy, A. & Kozerke, S. 5D flow tensor MRI to efficiently map Reynolds stresses of aortic blood flow in-vivo. *Sci. Rep.* **9**, 1–12 (2019).
36. Garreau, M. *et al.* Accelerated sequences of 4D Flow MRI using GRAPPA and compressed sensing: A comparison against conventional MRI and computational fluid dynamics. *Magn. Reson. Med.* **88**, 2432–2446 (2022).
37. Rutkowski, D. R., Roldán-Alzate, A. & Johnson, K. M. Enhancement of cerebrovascular 4D Flow MRI velocity fields using machine learning and computational fluid dynamics simulation data. *Sci. Rep.* **11**, 10240 (2021).

38. Miyazaki, S. *et al.* Validation of numerical simulation methods in aortic arch using 4D Flow MRI. *Heart Vessels* **32**, 1032–1044 (2017).
39. Romarowski, R. M., Lefieux, A., Morganti, S., Veneziani, A. & Auricchio, F. Patient-specific CFD modelling in the thoracic aorta with PC-MRI-based boundary conditions: A least-square three-element Windkessel approach. *Int. J. Numer. Method. Biomed. Eng.* **34**, 1–21 (2018).
40. Ha, H. *et al.* Assessment of turbulent viscous stress using ICOSA 4D Flow MRI for prediction of hemodynamic blood damage. *Sci. Rep.* **6**, 1–14 (2016).
41. Ferdian, E. *et al.* 4DFlowNet: Super-resolution 4D Flow MRI using deep learning and computational fluid dynamics. *Front. Phys.* **8**, 138 (2020).
42. Ferdian, E. *et al.* Cerebrovascular super-resolution 4D Flow MRI—Sequential combination of resolution enhancement by deep learning and physics-informed image processing to non-invasively quantify intracranial velocity, flow, and relative pressure. *Med. Image Anal.* **88**, 102831 (2023).
43. Petersson, S., Dyverfeldt, P., Gårdhagen, R., Karlsson, M. & Ebbers, T. Simulation of phase contrast MRI of turbulent flow. *Magn. Reson. Med.* **64**, 1039–1046 (2010).
44. Puiseux, T., Sewonu, A., Moreno, R., Mendez, S. & Nicoud, F. Numerical simulation of time-resolved 3D phase-contrast magnetic resonance imaging. *PLoS ONE* **16**, e0248816 (2021).
45. Steinman, D. A., Ethier, C. R. & Rutt, B. K. Combined analysis of spatial and velocity displacement artifacts in phase contrast measurements of complex flows. *J. Magn. Reson. Imaging* **7**, 339–346 (1997).
46. Ha, H. *et al.* Estimation of turbulent kinetic energy using 4D phase-contrast MRI: Effect of scan parameters and target vessel size. *Magn. Reson. Imaging* **34**, 715–723 (2016).
47. Cheng, J. Y. *et al.* Comprehensive motion-compensated highly accelerated 4D Flow MRI with ferumoxytol enhancement for pediatric congenital heart disease. *J. Magn. Reson. Imaging* **43**, 1355–1368 (2016).
48. Trzasko, J., Armando, M. & Eric, B. Local versus global low-rank promotion in dynamic mri series reconstruction. *Proc. Int. Symp. Magn. Reson. Med.* **19**, 4371 (2011).
49. Dirix, P., Buoso, S., Peper, E. S. & Kozerke, S. Synthesis of patient-specific multipoint 4D Flow MRI data of turbulent aortic flow downstream of stenotic valves. *Sci. Rep.* **12**, 16004 (2022).
50. Guerquin-Kern, M., Lejeune, L., Pruessmann, K. P. & Unser, M. Realistic analytical phantoms for parallel magnetic resonance imaging. *IEEE Trans. Med. Imaging* **31**, 626–636 (2012).
51. Baumgartner, H. *et al.* Recommendations on the echocardiographic assessment of aortic valve stenosis: A focused update from the European Association of Cardiovascular Imaging and the American Society of Echocardiography. *J. Am. Soc. Echocardiogr.* **30**, 372–392 (2017).
52. Busch, J., Giese, D. & Kozerke, S. Image-based background phase error correction in 4D Flow MRI revisited. *J. Magn. Reson. Imaging* **46**, 1516–1525 (2017).
53. Uecker, M. *et al.* Berkeley advanced reconstruction toolbox. *Proc. Int. Soc. Mag. Reson. Med.* **23**, 2486 (2015).
54. Ma, L. E. *et al.* 5D flow MRI: A fully self-gated, free-running framework for cardiac and respiratory motion-resolved 3D hemodynamics. *Radiol. Cardiothorac. Imaging* **2**, e200219 (2020).
55. Vishnevskiy, V., Gass, T., Szekely, G., Tanner, C. & Goksel, O. Isotropic total variation regularization of displacements in parametric image registration. *IEEE Trans. Med. Imaging* **36**, 385–395 (2017).
56. Wang, Z., Bovik, A. C., Sheikh, H. R. & Simoncelli, E. P. Image quality assessment: From error visibility to structural similarity. *IEEE Trans. Image Process.* **13**, 600–612 (2004).
57. Dyverfeldt, P. & Ebbers, T. Comparison of respiratory motion suppression techniques for 4D Flow MRI. *Magn. Reson. Med.* **78**, 1877–1882 (2017).
58. Kolbitsch, C. *et al.* Respiratory motion corrected 4D Flow using golden radial phase encoding. *Magn. Reson. Med.* **83**, 635–644 (2020).
59. Gülan, U., Binter, C., Kozerke, S. & Holzner, M. Shear-scaling-based approach for irreversible energy loss estimation in stenotic aortic flow—An in vitro study. *J. Biomech.* **56**, 89–96 (2017).
60. Ha, H., Kvitting, J., Dyverfeldt, P. & Ebbers, T. Validation of pressure drop assessment using 4D Flow MRI-based turbulence production in various shapes of aortic stenoses. *Magn. Reson. Med.* **81**, 893–906 (2019).
61. Dillinger, H., Walheim, J. & Kozerke, S. On the limitations of echo planar 4D Flow MRI. *Magn. Reson. Med.* **84**, 1806–1816 (2020).
62. Hazra, A., Lube, G. & Raumer, H.-G. Numerical simulation of Bloch equations for dynamic magnetic resonance imaging. *Appl. Numer. Math.* **123**, 241–255 (2018).
63. Stöcker, T., Vahedipour, K. & Pflugfelder, D. *JEMRIS*. https://www.jemris.org/.
64. Weine, J. & McGrath, C. *CMRsim*. https://people.ee.ethz.ch/~jweine/cmrsim/latest/index.html.
65. Braig, M. *et al.* Analysis of accelerated 4D Flow MRI in the murine aorta by radial acquisition and compressed sensing reconstruction. *NMR Biomed.* **33**, e4394 (2020).
66. Dyvorne, H. *et al.* Abdominal 4D Flow MR imaging in a breath hold: Combination of spiral sampling and dynamic compressed sensing for highly accelerated acquisition. *Radiology* **275**, 245–254 (2015).
67. Hess, A. T. *et al.* Aortic 4D Flow: Quantification of signal-to-noise ratio as a function of field strength and contrast enhancement for 1.5T, 3T, and 7T. *Magn. Reson. Med.* **73**, 1864–1871 (2015).

Acknowledgements

Author contributions

P.D., S.B. and S.K. designed the study and discussed the results; P.D. and S.B. developed the simulation framework; P.D. wrote the original draft. All authors participated in revising the manuscript and read and approved the final manuscript.

Competing interests

The authors declare no competing interests.

Additional information

Supplementary Information The online version contains supplementary material available at https://doi.org/10.1038/s41598-024-70449-9.

Correspondence and requests for materials should be addressed to P.D.